Large-Eddy / Reynolds-Averaged Navier-Stokes Simulations of a Dual-Mode Scramjet Combustor

Jesse A. Fulton[1], Jack R. Edwards[2], Hassan A. Hassan[3],
North Carolina State University, Mechanical and Aerospace Engineering, Raleigh, NC 27695
Robert Rockwell[4], Christopher Goyne[5], Jim McDaniel[6], Chad Smith[7]
University of Virginia, Mechanical and Aerospace Engineering, Charlottesville, VA 22904
Andrew Cutler[8]
The George Washington University, Mechanical and Aerospace Engineering, Newport News, VA 23602
Craig Johansen[9]
University of Calgary, Mechanical and Manufacturing Engineering, Calgary, AB, Canada
Paul. M. Danehy[10]
NASA Langley Research Center, Hampton, VA, 23681
Toshinori Kouchi[11]
Tohoku University, Aerospace Engineering, Sendai, Japan

Numerical simulations of reacting and non-reacting flows within a scramjet combustor configuration experimentally mapped at the University of Virginia's Scramjet Combustion Facility (operating with Configuration "A") are described in this paper. Reynolds-Averaged Navier-Stokes (RANS) and hybrid Large Eddy Simulation / Reynolds-Averaged Navier-Stokes (LES / RANS) methods are utilized, with the intent of comparing essentially 'blind' predictions with results from non-intrusive flow-field measurement methods including coherent anti-Stokes Raman spectroscopy (CARS), hydroxyl radical planar laser-induced fluorescence (OH-PLIF), stereoscopic particle image velocimetry (SPIV), wavelength modulation spectroscopy (WMS), and focusing Schlieren. NC State's REACTMB solver was used both for RANS and LES / RANS, along with a 9-species, 19-reaction H_2-air kinetics mechanism by Jachimowski. Inviscid fluxes were evaluated using Edwards' LDFSS flux-splitting scheme, and the Menter BSL turbulence model was utilized in both full-domain RANS simulations and as the unsteady RANS portion of the LES / RANS closure. Simulations were executed and compared with experiment at two equivalence ratios, $\Phi = 0.17$ and $\Phi = 0.34$. Results show that the $\Phi = 0.17$ flame is hotter near the injector while the $\Phi = 0.34$ flame is displaced further downstream in the combustor, though it is still anchored to the injector. Reactant mixing was predicted to be much better at the lower equivalence ratio. The LES / RANS model appears to predict lower overall heat release compared to RANS (at least for $\Phi = 0.17$), and its capability to capture the direct effects of larger turbulent eddies leads to much better predictions of reactant mixing and combustion in the flame stabilization region downstream of the fuel injector. Numerical results from the LES/RANS model also show very good agreement with OH-PLIF and SPIV measurements. An un-damped long-wave oscillation of the pre-combustion shock train, which caused convergence problems in some RANS simulations, was also captured in LES / RANS simulations, which were able to accommodate its effects accurately.

---

[1] Graduate research assistant, Student Member AIAA
[2] Professor, Associate Fellow AIAA
[3] Professor, Fellow AIAA
[4] Senior Scientist, Senior Member AIAA
[5] Research Associate Professor, Associate Fellow AIAA
[6] Professor, Associate Fellow AIAA
[7] Graduate Research Assistant, Student Member AIAA
[8] Professor, Associate Fellow AIAA
[9] Assistant Professor, Senior Member AIAA
[10] Research Scientist. Associate Fellow AIAA
[11] Assistant Professor. Member AIAA

I.   Introduction

The research and design of a hypersonic propulsion system is a valuable goal for the aerospace industry, as it will yield a vastly efficient connection between conventional flight and orbital access. However, despite its standing for decades as a primary objective for many engineers and scientists, hypersonic flight in practice has been often regarded as more of a necessary evil, as in the case of planetary reentry after an orbital flight, and less of a realm to be explored. The development of an engine that can operate in the precise, hostile, and unforgiving environment of hypersonic flow hinges on cooperative efforts of the many different disciplines in the aerospace industry. Given the difficulties in conducting ground-test measurements at conditions relevant to hypersonic propulsion, numerical simulations have played a key role in advancing the understanding of the relevant physical phenomena. Such numerical simulations require validation through comparisons with experimental results that can be obtained in this flow regime; otherwise, the simulations cannot be proven trustworthy. The current research effort is to develop new generations of advanced numerical simulation tools to be used toward this purpose.

The state of the art in high-speed flow simulation is currently solution of the Reynolds-Averaged Navier-Stokes (RANS) equations [1]. The RANS equations are formulated by time-averaging the standard Navier-Stokes equations. By doing this, time-dependent turbulent fluctuations are eliminated from the resulting set of equations, and so the only variables left to be resolved are those of the mean flow. The turbulent effects remaining to be solved, such as Reynolds stresses, are determined using one of a variety of turbulence models. These techniques have been categorized as 'Generation I' techniques. A significant disadvantage of RANS simulation that is a result of modeling all turbulence is that it cannot distinguish between phenomena which dominate in one scale of turbulence or another (i.e., turbulent mixing, which is usually weighted toward the large scales of turbulence [2]). More sophisticated methods such as Generation II (hybrid LES/RANS) and Generation III (LES) alleviate this problem by resolving the larger scales of turbulence, but in doing so, they also require much higher mesh resolutions relative to RANS grids in order to capture these scales. The resolution of some of the unsteady turbulent structures also makes it necessary to run these higher-fidelity simulations time-accurately, using a global time step instead of a local one as in RANS simulations. Another difficulty in the development of CFD methodologies suited for high-speed flows is the relatively sparse amount of experimental data available with which numerical codes can be compared and validated. Thus, the development of an understanding of hypersonic flows is two-pronged: the development of higher-fidelity numerical solution methodologies and a database of high-quality experimental data so that these methodologies can be refined and validated.

The National Center for Hypersonic Combined-Cycle Propulsion (NCHCCP) is a program developed to help bridge this gap and has allowed intense collaboration between numerical and experimental groups in order for a deeper understanding of hypersonic propulsion to be developed [1]. One of the primary goals in this center is to develop Generation II and III techniques of numerical simulation that are well-suited to the problem of hypersonic propulsion. NC State University is conducting RANS and hybrid LES/RANS simulations of reacting and non-reacting flows within various scramjet combustor designs tested within the University of Virginia's continuous-flow dual-mode Scramjet Combustion Facility (SCF). Various non-intrusive flow diagnostics are being applied to gather experimental data suitable for assessing the performance of Generation I, II, and III simulation techniques.

II.   Background

Despite the ongoing challenges that hypersonic propulsion brings to the CFD community, there have been successful computational developments in the recent past. There are currently a number of production-level codes used for high-speed reacting flows that have been developed and are maintained by a variety of governmental and commercial groups [1]. NASA has developed the SPARK, LARCK, and VULCAN codes which have been used for a large number of simulations. NASA has also collaborated with the US Air Force and Boeing for the development of the Wind-US flow solver. Other flow solvers that have been successful in a variety of applications include Aerosoft's GASP, Metacomp Technologies' CFD++, and NC State University's own REACTMB series. All of these current flow solvers generally fall within the Generation I (RANS) category, though some can utilize higher-fidelity models.

These numerical simulation tools have proven satisfactory for almost all recent research in hypersonic propulsion. Some of the highest-profile hypersonic and high-speed propulsion projects which utilized these tools are the Space Shuttle Main Engine (SSME), the National Aerospace Plane (NASP), NASA's Hyper-X, the University of

Queensland's HyShot program, the USAF's Scramjet Engine Demonstrator, and the recently successful X-51 hypersonic research airplane.

Generation I RANS methods have also been used in earlier simulations of the SCF at the University of Virginia. Goyne et al. [3] have conducted separate RANS simulations of the nozzle and combustor for both nonreactive mixing and reacting flows using NASA's VULCAN flow solver. Their results indicated that the simulations generally under-predicted turbulent mixing and heat release. More recently, work done by Georgiadis et al. [4] focused on the validation of the Wind-US flow solver in the context of hypersonic reactive flows, using the SCF as one of their test cases. The main focus of their work was a parametric study of turbulence / transition, heat transfer, and kinetics modeling in order to determine which methods were most suited for scramjet combustor flows. Vyas et al. [5] also used Wind-US in order to study the effects of vitiation on the operation of the SCF at a variety of equivalence ratios. Their simulations successfully determined that there was a shift in ram / scram mode behavior between vitiated and un-vitiated cases at a particular midrange equivalence ratio. However, combustor and extender pressures were under-predicted at lower equivalence ratios; it was concluded from this that a variable Schmidt / Prandtl number turbulence model was necessary in order for RANS simulations to correctly predict flow behavior at a wide range of equivalence ratios. It should be mentioned that these earlier simulations were performed on an internal flowpath configuration of the SCF combustor that is different from the ones designed as part of the NCHCCP. Fulton, et al. [6] and Hassan, et al. [7] have performed RANS and LES/RANS simulations on two of the configurations built as part of the NCHCCP. These earlier simulations were conducted without benefit of detailed experimental data; the present paper compares new computational predictions with a variety of experimental results collected on one scramjet combustor configuration (Configuration A, described later). The computations were essentially performed in a 'blind' manner, in that only wall-pressure distributions at one equivalence ratio were available before the calculations were completed. As such, they represent a first-cut evaluation of the predictive capabilities of the models, without any adjustments being made to enable better agreement with experiment.

III.   Facility

The University of Virginia's Supersonic Combustion Facility (SCF) (see Figure 1) is a small-scale direct-connect ram/scramjet combustor apparatus whose operation is designed to simulate flight conditions at Mach 5 enthalpy. [1] It is vertically mounted and consists of an inlet nozzle, constant-area isolator, combustor, and extender, from which the exhaust gases are vented to the atmosphere. The Mach 2 inlet nozzle, located upstream of the isolator and combustor apparatus, is responsible for bringing the incoming airflow up to the speeds at the isolator entrance that would normally be seen during low hypersonic flight, after the freestream air has been slowed and compressed in the inlet section of a hypersonic aircraft. In addition, the incoming air is compressed to a stagnation pressure of roughly 300 kPa using an oil-free compressor, and a 300 kW, 14-stage electrical resistance heater raises the stagnation temperature to 1200 K without introducing flow vitiates – a significant advantage of this facility. The experimental facility is also fitted with a system of coolant lines, thermocouples, and pressure transducers for cooling of the SCF and data measurement. The facility is capable of operating continuously for long durations, limited only by the available fuel supply during combusting experiments.

For the current investigations, hydrogen was used as the fuel for the SCF. The fuel is introduced into the airflow via a single, wall-mounted, unswept, 10º raised compression ramp injector. The fuel-injection nozzle is a converging-diverging conical design that accelerates the fuel to approximately Mach 1.7 at its exit. At lower equivalence ratios, the facility operates in scramjet mode; as the equivalence ratio is increased, it transitions to dual-mode operation and then to ram operation as the precombustion shock train moves upstream from the combustor and eventually stabilizes in the isolator region.

There have been a number of revisions to the flowpath configuration of the SCF; for the purposes of this paper, all experiments and simulations have been performed on an arrangement which has been named Configuration A. The general layout of Configuration A is shown in Figure 2. The isolator in this layout is much shorter than the length that was used in previous studies. The compression ramp and injector mark the entrance to the combustor, where a 2.9º divergence on the injector wall also begins. This divergence has been placed further upstream than in older configurations in anticipation of future experiments at higher equivalence ratios and with hydrocarbon fuels.

In conjunction with NC State's CFD computations, high-fidelity experimental data is being gathered from the SCF experiments using various non-intrusive measurement techniques, such as wavelength modulation spectroscopy (WMS) (Stanford University), coherent anti-Stokes Raman spectroscopy (CARS) (George Washington University), OH planar laser induced fluorescence (OH-PLIF) (NASA Langley, University of Calgary, and the

George Washington University), stereoscopic planar laser velocimetry (SPIV) (University of Virginia), and focusing Schlieren (University of Virginia and Tohoku University). The SCF has been specially modified to permit measurements such as these at a large number of locations throughout the flowpath. This is the kind of data that will greatly assist evaluation of Generation I methodologies as well as in validation of higher-fidelity Generation II and III methodologies.

IV.   Numerical Formulation

NC State is using its REACTMB flow solver for its RANS and LES-RANS simulations. This code solves the Reynolds-Averaged (Favre-averaged for compressible flows) Navier-Stokes equations – expanded to accommodate reactive species production, depletion and transport – on multi-block structured meshes using finite volume methods. Hydrogen oxidation is modeled by a 9-species, 19-reaction reaction mechanism developed by Jachimowski [8]. The reactive source terms are evaluated using mean or filtered-mean data – no turbulence / chemistry interactions are modeled. For inviscid fluxes, Edwards' low diffusion flux splitting scheme (LDFSS) [9], extended to higher-order spatial accuracy using PPM (Piecewise Parabolic Method) or TVD (Total Variation Diminishing) reconstruction schemes applied to the primitive variables $W = [p_s, u, v, w, T, k, \omega]^T$, is used. Here, p_s is the partial pressure of species s, u, v, and w are the Cartesian velocity components, T is the temperature, k is the turbulence kinetic energy, and ω is the specific dissipation rate. For the LES/RANS simulations, it is necessary to reduce the numerical dissipation significantly in regions of high turbulence activity. This is accomplished by blending left- and right states determined from the PPM or TVD schemes with an averaging operator that yields a fourth-order central difference on uniform meshes. The blending function (Eq. 1) is the well-known vorticity / divergence function of Ducros, et al. [10]. In the present work, the Ducros switch is used with a TVD reconstruction – the scheme that results is referred to as LD-TVD for low-dissipation TVD.

$$f = \frac{(\nabla \cdot \vec{V})^2}{(\nabla \cdot \vec{V})^2 + |\omega|^2 + \varepsilon^2}, \quad \varepsilon = 1 \times 10^{-8} V_\infty / \max(\overline{\Delta x}, \overline{\Delta y}, \overline{\Delta z})$$

(1)

For the latest efforts, the Menter baseline (BSL) [11] turbulence model is used for steady RANS computations, after an initial study determined that this version predicted a more accurate shock train in the extender during nonreactive fuel-air mixing simulations. The Menter BSL model is also employed as the RANS component of the LES/RANS model, which is based on the work of Gieseking, et al. [12]. Here, the eddy viscosity provided by the Menter BSL model is blended with a subgrid model from Lenormand, et al. [13]:

$$\mu_t = \rho \left[(1 - \Gamma) \nu_{t,sgs} + \Gamma \frac{k}{\omega} \right]$$

(2)

The blending function Γ is generally designed to transition the model from RANS to LES approximately as the boundary layer shifts from its logarithmic to its wake-like structure.   The most recent model [12] introduces an outer-layer turbulence length scale into the argument for Γ in an attempt to remove a calibration procedure required in an earlier model:

$$\Gamma = \frac{1}{2} \left(1 - \tanh[15(\frac{1}{\lambda_N^2} - 1)] \right),$$

(3)

where

$$\lambda_N \equiv \frac{l_{outer}}{l_{inner}} = C_N \sqrt{\frac{10\nu\overline{\omega} + \overline{k} + \overline{k}_R}{C_\mu^{1/2} \overline{\omega} \omega}} / \kappa d = C_N \sqrt{10 + \frac{\overline{k} + \overline{k}_R}{\nu\overline{\omega}}} \frac{\sqrt{\nu}}{C_\mu^{1/4} \kappa d \sqrt{\omega}}$$

(4)

In this expression, $\overline{k}$ is the ensemble-averaged modeled turbulence kinetic energy, $\overline{k}_R$ is the ensemble-averaged resolved turbulence kinetic energy, ω and $\overline{\omega}$ are instantaneous and ensemble-averaged modeled turbulence frequencies, and d is the distance to the nearest wall. The combination of instantaneous and ensemble-averaged

data allows the RANS-to-LES transition position $\Gamma = 1/2$ to fluctuate about a mean value that is a function of the local, ensemble-averaged state of the flow. As it is dependent on both inner-layer and outer-layer length scale information, this model is more capable of adjusting to departures from local equilibrium, and a problem-specific selection of a model constant is not required.

In previous simulations conducted at NC State [6], the thermal wall boundary conditions for the mesh utilized a simple one-dimensional conjugate heat transfer model. This model solved for wall temperatures based on facility parameters and assuming all walls were made of stainless steel coated with a thin layer of zirconia. More recently, thermal response analyses carried out by Bob Rockwell of UVa [14] using thermal inputs extracted from NCSU's RANS results have determined that it is appropriate to set wall temperatures to fixed values (discussed further in the next section).

V.   Calculation Details

The LES/RANS solution method must be initialized from a converged RANS solution. Consequently, a mesh that was sufficient for LES/RANS simulations as well as RANS simulations was developed. The internal flowpath geometry of the SCF presents some practical difficulties related to numerical computations – mainly regarding the mesh size variation and distortion needed to adequately resolve the entire flow domain. This difficulty was compounded by the fact that the hybrid LES/RANS solution requires global time stepping, which is limited by the minimum cell size. Steps were therefore taken to mitigate these difficulties as much as possible in order to produce rapid solutions without unnecessary degrees of freedom. In previous simulations using RANS techniques and a much coarser grid [6], the small channel for the fuel injector was included in the combustor mesh, creating a region of cells that were much finer than the rest of the grid. This was not a problem at the time since steady RANS methods were being used, which were not as limited by minimum cell size. Although the present grid is overall much finer than the mesh used in the older RANS simulations, meshing of the injection channel would still have resulted in cells that were much smaller than the remainder of the combustor grid. Since the allowable time step in LES/RANS simulations is directly related to minimum cell size, the region of very small cells in the fuel injection channel would have made the time step prohibitively short. As a result, the internal injection channels rendered in the coarser RANS meshes were removed for the present grids, and a solution for the flow-field variables at the injector exit was taken from a previous coarse-mesh RANS solution and interpolated to the finer mesh to provide a steady-state boundary condition at the injection face of the ramp.

The slow relaxation time for the large region of subsonic flow upstream of the air-stream nozzle severely lengthens convergence time, while the isolator decouples this flow from the rest of the combustor. Consequently, the entire nozzle domain is split off from that of the combustor. By doing this, the nozzle flow can be solved one time using RANS methods and its steady-state outflow profile extracted and introduced as a mean inflow condition for RANS and LES-RANS solutions of the combustor domain. This assumes that pressure perturbations resulting from combustion do not feed forward to the inflow boundary. Available experimental data and current simulation results indicate that this assumption is adequate. The air-stream nozzle stagnation pressure in the simulations was set to 296 kPa, and the air-stream nozzle stagnation temperature was fixed at 1200 K. Cutler, et al. [17] have determined that the SCF facility exhibits a variation in static temperature (ranging between +50 K and -100 K) from the expected inflow temperature of 667 K at the combustor entrance. They have also determined that the nitrogen in the inflow exhibits some departure from thermal equilibrium. Neither of these observed effects were included in the present simulations. Also, while it is possible to force the generation of realistic turbulent structures within the inflow channel boundary layers using recycling / rescaling methods [15], it was found that the boundary layer was too thin and the mesh too coarse to sustain such structures. As such, no such forcing was applied for the LES/RANS simulations.

In earlier RANS and LES/RANS simulations [6], the extender exit was simply treated as a combined supersonic/subsonic exit boundary condition: if the flow was subsonic, the exit pressure was set to ambient levels, and if supersonic, the pressure was extrapolated from the interior cells. Parallel flow was enforced over the entire exit plane. It was later found that this exit condition was not always sufficient to ensure that the exit pressure matched the ambient level and sometimes caused unrealistic shock structures to form just inside or at the exit. The current mesh has been modified to include a 'dump region' that allows the flow at the end of the combustor to exit more naturally. The outflow pressure condition is applied at the end of the dump region. A steady 25 m/s co-flow of room-temperature air is enforced at the inlet of the dump region, and a symmetry condition is enforced on the other boundaries of the dump region Since the only purpose of the dump region is to allow flow to relax to the ambient pressure level, it was created with as few mesh cells as possible, which are highly skewed. Figures 3 and 4 show the mesh used for LES/RANS and RANS simulations and the boundary conditions enforced. The combustor grid

contains about 33 million cells and the dump region contains about 1.75 million cells. The nozzle grid (not shown) contains about 17.8 million cells. The minimum mesh distance next to solid surfaces was set to 0.005 mm; far from walls in the mesh interior, the maximum mesh spacing was no greater than about 0.35 mm.

As mentioned before, the combustor walls enforce a no-slip condition and a fixed wall temperature of 600 K everywhere. This temperature was found to closely match experimental measurements as well as thermal response analyses. However, for combusting runs, the temperature along a small strip of wall immediately downstream of the injector and the ramp injector back plane was set to 1000 K. This mimics the effect of a zirconia coating in insulating the walls in this region. Experimental measurements confirm that the wall temperatures in this region of the combustor are elevated by 200-300 K.

Initialization of simulations began with reaching a converged steady-state RANS solution for the nozzle mesh with only air. Convergence of RANS simulations was determined mainly by monitoring mass inflow and outflow rates until they reached a balanced condition. Once the nozzle solution was obtained, its outflow was extracted and used as a steady boundary condition for both RANS and LES/RANS simulations of the combustor. In order to initialize the LES/RANS combustor simulation, a RANS solution for the combustor must first be obtained. Startup of RANS combustor simulations involved first initializing properties in the combustor using a basic linear transition from inflow to outflow states. At this time, reactions were turned off while fuel was introduced into the combustor in order to generate a 'cold-flow' or mixing solution. Once convergence was obtained, reactions were then turned on and activation energies lowered to initiate combustion; in addition, thermal boundary conditions were changed to adiabatic in order to retain heat in the combustor and aid in ignition. Once ignition was sustained, activation energies and fixed thermal boundary conditions were restored and the reactive solution was allowed to converge. In practice, it was found that a completely steady flow in the combustor could not be attained for most reactive cases, as the RANS solutions exhibited a long-cycle un-damped oscillation of mass flow rates. This was attributed to an oscillation of the combustion shock train caused by (and influencing) fluctuations in the position of maximum heat release.

LES/RANS simulations of the reactive case at $\Phi = 0.34$ and the mixing-only case at $\Phi = 0.17$ were initiated by simply restarting from the converged mixing or reactive RANS solution with the LES/RANS switching function enabled, the LD-TVD scheme invoked, and global time stepping turned on. The LES/RANS solutions were evolved for four transit times, where one transit time is defined as the time it takes for a fluid particle moving at inflow velocity to transit the length of the combustor, to purge initial transients and to complete the transition from RANS to LES/RANS. Statistics (i.e., time-averages) of the instantaneous solutions were taken for at least another eight transit times. The $\Phi = 0.34$ reactive LES/RANS solution obtained after four transit times was used to initialize the $\Phi = 0.17$ LES/RANS solution. Attempts to start this lower Φ case from a converged RANS solution led to flame detachment from the injector face and eventual flame blowout. It should be mentioned that in the experiment, combustion is also initiated at a higher equivalence ratio ($\sim0.4 - 0.45$) by reducing the air stagnation pressure until the extender shock train moves upstream and ignites the hydrogen gas. From that point, the air stagnation pressure is raised to its target value (nominally 300 kPa) and the fuel stagnation pressure adjusted to meet the desired equivalence ratio.

VI. Experimental Measurement Techniques

The following is an abbreviated description of the various diagnostic techniques being applied to interrogate the reactive flow within the Configuration A combustor. More complete descriptions of some of the techniques may be found in companion papers [14, 16, 17, 20].

CARS (coherent anti-Stokes Raman scattering)

Coherent anti-Stokes Raman spectroscopy (CARS) is a non-linear spectroscopic technique in which three laser beams, two pump beams and a Stokes beam, are focused and crossed at their focal point, and a fourth laser beam, known as the signal beam, is generated at the intersection through a four-wave mixing process. Resonances associated with Raman-active molecular rotational and rotational-vibrational transitions strengthen the CARS signal in a manner dependent on gas composition and temperature. The wavelength of excitation or "Raman shift" corresponds to the difference in energy between a pump beam and a Stokes beam (longer wavelength) photon. In the broadband CARS technique one of the laser beams, the Stokes beam, is spectrally broad whereas the other pump beams are spectrally narrow, and this enables multiple resonances to be excited simultaneously. The signal beam is spectrally broad and carries with it the spectral signature of the gases present (over some range of wavelengths). This signal beam is dispersed by a spectrometer and spectra are compared to analytical spectral models to obtain

information on composition and temperature. Further details may be found in the companion papers by Magnotti [16] and Cutler, et al. [17]. CARS techniques were used to provide quantitative mean temperature, H_2 mole fraction, N_2 mole fraction, and O_2 mole fraction measurements at specific locations within four y-z planes: x/H = -10.4 (inflow), x/H = 6, x/H = 12, and x/H = 18. The technique also provides a wide range of statistics of fluctuations in the reactive scalars; however, only mean-flow CARS results obtained past the injector exit (x/H = 0) at combusting conditions corresponding to $\Phi = 0.17$ are compared to the present computations.

OH-PLIF (planar laser induced fluorescence)

Planar laser-induced fluorescence (PLIF) from the hydroxyl (OH) radical was used to visualize the flame structure and residual burnt gases downstream of the fuel injector. Tuneable ultra-violet (UV) light near 283 nm was used to excite the OH molecules through the $A^2\Sigma^+ \leftarrow X^2\Pi_\Omega(1,0)$ $Q_1(8)$ transition. This transition was previously used by O'Byrne et al. [18] to obtain OH PLIF measurements of supersonic combustion in the T-3 shock tunnel facility. The $Q_1(8)$ transition is well isolated and is relatively insensitive to changes in temperature, so that the PLIF signal is roughly proportional to the local concentration of OH. Pulses of UV light were produced from a frequency-doubled pulsed dye laser (Spectra-Physics PDL2), which was pumped by a fraction of the 532 nm output from an injection-seeded Spectra-Physics Pro-350 Nd:YAG laser. UV turning prisms and mirrors were used to guide the beam onto a two-component motorized translation stage. The beam was then formed into a sheet using a cylindrical and spherical lens, delivering approximately 1.7 mJ/pulse of UV light into the test section. The laser sheet was oriented horizontally in the vertical flow. Two windows were mounted on opposite sides of the duct. One window was used for the incoming laser sheet and the opposite window was used for viewing the fluorescence by the camera. The camera was a Princeton Instruments PiMAX II intensified CCD camera that framed at a rate of 10 Hz. The camera was equipped with a UV Nikkor 105 mm focal length, f/4.5 lens with filters to block the laser's wavelength and transmit the OH fluorescence. The camera was orientated at an angle relative to the laser sheet, so a Scheimpflug adapter was used to focus the image onto the CCD. Both the laser sheet and camera were translated in the streamwise direction to obtain OH PLIF images along the entire length of the duct. The OH images presented in this work are un-processed and were obtained at one streamwise location (x/H = 12) and at an equivalence ratio of $\Phi = 0.17$.

Focusing Schlieren

Focusing Schlieren was used to visualize the shock and large-scale turbulent structures around the fuel injector. We used Weinstein's modern focusing-Schlieren system [19] using a Fresnel lens and a high-quality camera lens (85 mm-focal length and f/1.4). The camera lens was put very close to the tunnel window to achieve a narrow depth of the field. The depth of the field for the present system was experimentally determined using a 1 mm-diameter over-expanded supersonic jet. It was roughly ± 5 mm. Such a narrow depth of field mitigated the thermal distortion of the tunnel windows when the tunnel heating up. The light source was a frequency-doubled Nd: YAG laser with the pulse width of 10 ns. The short duration pulse light captured the instantaneous structure of the flowfield. The laser beam was first diffused by foaming polypropylene sheets to make an extended light source and collected by the Fresnel lens to increase the light-collection efficiency. The diffused beam illuminated a source grid that consisted of multiple, alternating dark bands and clear aperture. The source grid was made photographically and was placed to emphasize density gradients in the streamwise direction. Light from the source grid was focused by the camera lens. The lens was placed 110 mm from the object plane. The Schlieren lens formed an image of the source grid and that of the object plane of the combustor center in each plane optically conjugate to them. The cutoff grid was made by photographically exposing and developing a negative image of the source grid on high-contrast lithographic film. Another Fresnel lens was placed on the imaging plane and the lens relayed the Schlieren image to CCD camera. After image acquisition, the images were post-processing by nonlinear unshaped masking operator to enhance the edge of the structures and to eliminate uneven exposure due to the thermal distortion of the windows.

Stereoscopic Particle Image Velocimetry (SPIV)

Particle Image Velocimetry (PIV) is an optically based, non-intrusive measurement technique for determining velocity from the displacement of particles that have been added to a flow. Measurement of velocity is accomplished by capturing images of the particles at two subsequent times, giving particle displacements over the time between the images. Particles must be carefully chosen when conducting a PIV experiment, particularly for measurement of supersonic flows, to ensure that the tracer particles accurately track the flow and therefore

accurately represent the velocity of the flow under investigation. For the simple two-dimensional (2D) PIV technique, one camera is positioned to view a portion of the flow illuminated by a laser light sheet. The two particle images necessary for determining displacement are recorded using consecutive pulses of the laser and the known time between these laser pulses is used to calculate velocity from displacement measurements. The necessary particle displacements are determined by dividing the recorded images into smaller sub-regions and using statistical correlation to determine particle motion within each sub-region.

An extension of the basic PIV technique, Stereoscopic Particle Image Velocimetry (SPIV) employs two cameras which view the flow from different perspectives. The same physical principles and statistical correlation methods apply to SPIV as in the basic (two-component) PIV method; however, the second perspective allows determination of the third velocity component, which is perpendicular to the laser sheet. For SPIV, two-component velocity vectors are first determined for each of the two cameras and these vectors are then combined using a predetermined image-to-world mapping function to produce a three-component velocity field. The SPIV measurements of the scramjet combustor flow field, presented here, were completed by placing two cameras on the same side of the laser sheet, each angled at 30 degrees from perpendicular to the sheet. The laser sheet was collimated in width so it could be passed through tunnel windows, with the sheet oriented perpendicular to the axial flow direction. The sheet was set to a thickness of 2.5 mm and the time between laser pulses was 400 nsec. For these measurements, the field of view of each camera extended beyond the cross-section of the combustor duct, however, only the fuel was seeded so that three-component velocity vectors could only be obtained in the area of the fuel plume. The particles chosen for this study were 0.25 micrometer diameter silicon dioxide particles. These tracer particles have previously been studied and are expected to accurately track the flow in question, and at the same time, survive the high temperatures produced by the combusting hydrogen fuel.

Wall Pressure and Temperature Measurements

A NetScannerTM pressure scanner and remote NetScanner TM thermocouple unit were used to acquire wall pressures and temperatures along the centerline of the fuel injector wall in the scramjet flowpath. Typically, a scan of 20 samples was acquired over 2 sec. at a sample rate of 10 Hz for each pressure tap and thermocouple. This data was then averaged and normalized by the measured pressure at the most upstream pressure tap (0.25 in. downstream of the facility nozzle exit) prior to plotting. Pressure and temperature were typically measured to within ±0.5% and average quantities typically had a 95% confidence interval of no more than ±1.5%. [14]

Other Measurement Techniques

In addition, wavelength modulation spectroscopy (WMS) techniques [20] have been applied by Stanford University researchers to obtain line-of-sight temperature and water mole fraction distributions at x/D = 6, 12, and 18 at $\Phi = 0.17$ and $\Phi = 0.34$. This data is still being analyzed, and no comparisons are presented in this paper.

VII.   Results

A. Flow Structure: Reactant Mixing without Combustion, Φ=0.17

Figure 5 shows plots of temperature and Fig. 6 shows Mach number on the centerplane of the combustor, which passes through the axial centerline of the flowpath, for a nonreactive run at $\Phi = 0.17$. (Figure 6 uses a color mapping that emphasizes the supersonic and subsonic regions of the flow.) Note that although the dump region is used in all simulations, the results of the simulations in that region are not shown. The three plots in each figure correspond to the LES-RANS instantaneous, LES-RANS time-averaged, and RANS solutions for fuel-air mixing at a 0.17 equivalence ratio. In all three cases there can be seen a 'swallowed' shock train initiated at the raised compression ramp and extending into the combustor (seen better in Figure 5) and a final shock train created as the flow compresses back to atmospheric pressure in the extender. Also visible is the hydrogen-gas fuel plume which occupies the upper region of the combustor. The Mach 1.7 injector nozzle is designed so that (for all equivalence ratios considered) the fuel supply pressure is high enough to cause the nozzle to operate in an underexpanded condition as the gaseous fuel exits the nozzle into the high-velocity, low-pressure core flow. This causes the fuel to expand rapidly, accelerating it to high Mach numbers and reducing its temperature to about 100 K in a barrel-shaped expansion region just outside the nozzle. (This behavior is also observed in reacting runs, mentioned later.) Further heating and expansion of this fuel plume as it travels downstream tends to displace and compress the surrounding air, which augments the aforementioned initial shock train. Since the fuel does not react in these mixing cases, it

also serves to cool the local flow, which can be easily seen in the temperature plots. In the instantaneous plot, the fuel-air interface just outside the injector can be seen as a shear layer which quickly destabilizes and breaks up the fuel jet, which then forms into a large collection of eddies, greatly enhancing mixing. There can also be seen an area of cold recirculating fuel occupying the leeward region of the compression ramp. In combusting operation, this recirculation zone is crucial to flameholding.

The flow of fuel in the combustor and the momentum deficit created in the wake of the injector effectively divide the combustor flow into two general regions that flow alongside each other. The 'mixing' region extends downstream of the injector and is characterized by high vorticity and fuel mass fractions; the 'core flow' region is a high-speed region mostly free of fuel and vorticity. In combusting cases, the reaction zone will occupy the mixing region of the combustor, though it will be much larger due to volumetric expansion during combustion. In the two-dimensional slices shown in Fig. 5, these two regions are simply the upper and lower portions of the combustor and extender. However, it must always be kept in mind that the flowpath is inherently three-dimensional due to the finite width of the compression ramp, and so in actuality the core flow region, when seen in cross-section, will be 'U-shaped' as it wraps around the mixing region (or reacting region in the combusting cases). There is also an extensive region of low-momentum, occasionally separated flow, near the end of the extender (x/H > 25). This larger portion of this region is located alongside the wall opposite the injector wall. The reduced separation along the injector wall is not surprising, as the additional momentum supplied by the fuel injection tends to delay separation despite the strong adverse pressure gradient and the compression of the shock train.

The shape of the fuel plumes in the RANS and LES-RANS time-averaged plots agree fairly well. The most significant differences between these two cases appear to be the shape and position of the initial and final shock trains.   Comparing with the RANS solution, it can be seen that there are slight differences in structure of the initial shock train. The apparently lower volumetric expansion and dispersal of the fuel plume seems to cause slightly higher flow velocities and less compression of the adjacent core flow in the RANS solution. At a location shown by the circled regions in Figure 5, an oblique shock reflects from the bottom wall. It can be seen that the RANS solution predicts greater boundary layer thickening due to this shock than the LES-RANS solutions, to the point that the reflected shock is distorted as a double shock. The amount of thickening is important as this boundary layer will influence the shape and position of the final shock train in the extender.

The extender shock train shows even more variation between plots. In the instantaneous LES-RANS solution these shocks are crisp and easily discernible, but can hardly be seen in the time-averaged plot, which instead shows a region of gradual temperature increase that begins much further upstream than the instantaneous plot. This means that the LES-RANS solution is predicting an unsteady, oscillatory final shock train and that averaging effects lead to the blurring of the image. The RANS solution, however, is not able to capture unsteady structures (since it assumes steady flow at convergence) and so depicts the final shock train as fixed at one location in the extender, slightly downstream of the beginning of final compression in the time-averaged LES-RANS case.

B: Comparisons with Experiment: Reactant Mixing without Combustion, Φ=0.17

Figure 7 compares the absolute static pressures along the upper injector wall for three cases: LES-RANS time-averaged, RANS, and experimentally measured values for this equivalence ratio. The initial ramp shock at x/H~-6 and the low-pressure recirculation region at x/H=0 are clearly seen. All cases show a minimum pressure at x/H~16, from which point pressures increase to atmospheric exit values in some fashion or another. The experimental profile is clearly more well-matched by the LES-RANS simulation in the combustor/extender despite its prediction of slightly lower values throughout the extender. This under-prediction of the pressure level in the extender indicates that the LES/RANS methodology under-predicts the displacement effect of the region of low-momentum fluid that forms due to shock interaction with the viscous layers developing on the tunnel walls. The RANS simulation predicts a jagged pressure-recovery distribution due to the presence of the final shock train in its fixed position.

The experimental runs indicate that pressures along the injector wall recover in a smooth fashion with no distinct shock jumps. Since the core flow coming into the extender is mostly supersonic and so must necessarily contain shocks to allow a pressure increase, this smooth nature can be due to two possibilities. The first is that, as in the LES-RANS time-averaged case, there is some oscillation of the extender shock train, thus smoothing out the individual jumps of each shock into a more uniform gradient. The other possibility is that there is a thick layer of subsonic flow between the shock train and the measurement wall. In this region, pressure information can propagate upstream and downstream, effectively smoothing out the measured pressure profile between the core region and the wall. It is most likely that the actual cause of the smooth recovery is a combination of these effects. Both phenomena can be seen clearly in the LES-RANS instantaneous and averaged centerplane plots of Mach number in Fig. 6.

However, the RANS solution predicts extensive flow separation on the lower wall but very little on the upper wall (see Fig. 6), and the steady-state RANS methods cannot capture large-scale shock oscillations. As a result, the pressure profile is sharper, with noticeable peaks and valleys corresponding to various (steady) shock interactions.

Figure 8 compares predicted velocity magnitude contours at x/H = 12 from the LES-RANS and RANS methods with experimental values obtained using stereoscopic PIV. (See Figure 2 for the relative location of this data plane in combustor.) The data field for the SPIV measurements is incomplete due to issues with the seeding apparatus; in this experiment, only the fuel stream was seeded and so the measurement only shows results in the injection plume. This is still sufficient to compare experimental and numerical results within this region. The full shape of the mixing and core flow regions is shown clearly in the numerical results in this figure, with the core flow region forming a 'U-shape' as stated previously and wrapping around the mixing region. One of the advantages of using a finite-width compression ramp is that it generates counter-rotating axial vortices as the flow compressed by the ramp spills over toward the adjacent lower-pressure regions on either side of the ramp. This vortex action is crucial to efficient and timely mixing of the fuel plume with the core flow. According to Figure 8, the RANS simulation predicts stronger vortex action at x/H=12 as shown by the larger heart-shaped fuel plume. However, the LES-RANS results match the SPIV measurements much better in terms of the shape and extent of the mixing region. There appears to be a significant asymmetry in the inner low-momentum region of the fuel plume in the experiment that is not shown in the computational results. Since only the fuel stream was seeded in this experiment, there is also the possibility of a slight 'velocity bias' in which the velocity of the fuel is seen more strongly than the velocity of the interacting core flow. This would be most significant in the mixing regions of the flow at the outer edges of the fuel plume.

Figure 9 compares instantaneous axial density-gradient contours along the X-Y centerplane with focusing Schlieren images for jet mixing without combustion at $\Phi = 0.17$. The solutions show that the initial response is a free-jet expansion followed by a re-compression through a single Mach disk. Good agreement with the experimental image is indicated.

C. Flow Structure: Reactant Mixing with Combustion, Φ=0.17 and Φ=0.34

Figures 10 and 11 are temperature and Mach number centerplane plots of reacting solutions for $\Phi=0.17$. Figures 12 and 13 are plots of the same for $\Phi=0.34$. It can be seen that there is a much larger amount of volumetric expansion due to the burning gases and this in turn creates a greater blockage to the core flow, compressing and decelerating it more than in the mixing case. In the $\Phi=0.17$ case, the flame is well-anchored to the injector recirculation zone for both LES-RANS and RANS simulations. The reaction zone reaches its peak temperature between x/H=20 and x/H=40. Unlike the mixing case, the entirety of the reaction zone is subsonic due to heat release; the core flow region remains supersonic. The combustor is therefore in dual-mode operation. The combustion of fuel in the reaction zone has caused the pressure rise in the extender of the mixing case to be redirected toward the inflow of the combustor, strengthening the initial shock train and eliminating the final one. The flow separation seen in the extender of the mixing cases has disappeared. In addition, the initial shock train appears slightly blurred in the LES-RANS time-averaged results compared to the instantaneous results, indicating that there is some amount of unsteadiness in the shock train position.

One interesting phenomena to note in Figure 11 is that the hydrogen jet appears to penetrate much further into the combustor flow than in the mixing case. It seems that the elevated pressures near the injector outlet due to combustion have considerably reduced the amount of jet under-expansion, which appears to have focused the hydrogen jet much better. Multiple Mach barrels can be seen trailing from the injector, indicating a good pressure match between injector and combustor.

However, this fuel jet can be seen to differ appreciably between the LES-RANS averaged and RANS cases in Figures 10 and 11. In the LES-RANS case, the jet is almost perfectly straight; in the RANS, it is visibly deflected towards the core flow and seems to have lost some of its directional strength by this. Accompanying this pattern is a much stronger initial shock train in the RANS solution just downstream of injection, almost coalescing into a normal shock at x/H~6. This indicates that the volumetric expansion of reacting flow is much more abrupt in the RANS solution, pointing to greater heat release, faster combustion, and faster mixing. This highlights a fundamental difference between RANS and LES methods. Our RANS methods model turbulent mixing indirectly (using gradient diffusion assumptions) and assume laminar chemistry in the determination of reaction rates; the ability of LES to resolve some larger scales of turbulence means that it can use this information to calculate mixing rates more accurately as well as the effects of the resolved scales on flame propagation. The end result is a more complex mixing profile and lower reaction rates and heat release due to the influences of high turbulent strain rates. Figures 10 and 11 reinforce this.

Figures 12 and 13 reveal a rather counter-intuitive result for the Φ=0.34 case: for a higher fuel flow, the combustor flame appears weaker and more detached from the injector. For both LES-RANS and RANS results, the region of highest flame temperature has moved to a region between x/H=40 and beyond the extender exit. The actual shape of the reacting and core flow regions does not appear to have changed very much from the lower equivalence ratio, however. The initial shock train has become stronger, indicating that the degree of core-flow blockage due to volumetric expansion of the reacting plume has been increased. The instantaneous LES-RANS plot in Figure 13 indicates a region of flow separation on the wall opposite the injector within the shock train. This is an indicator of shock train movement in the upstream direction, which is actually part of an undamped long-wave oscillation of the entire shock train. Therefore, LES-RANS simulations predict combustion operation to be inherently unsteady. Since the RANS solution method assumes the converged solution to be steady-state, this casts some doubt on the validity of steady RANS simulations for this configuration. In fact, the RANS simulation used to create the plots seen in Figures 12 and 13 did contain some lasting oscillations in the residual; in other words, the solution never did quite reach a steady state. The shock-train-induced flow separation seen in Figure 13 gives strong evidence that this unsteadiness is once again due to shock-train oscillation. From this it seems that RANS simulations would need to be performed in a time-resolved manner in order to capture these large-scale unsteady phenomena more accurately.

Figure 14 more closely examines the instantaneous LES/RANS flow structure for both equivalence ratios using an isosurface of H_2 mass fraction (=0.1) in grey (uncolored) and an isosurface of temperature (=2200 K) colored by H_2O mass fraction. The displacement of the hot part of flame further downstream for the 0.34 equivalence ratio is clearly seen here. Destabilization and breakup of the fuel jet occurs more readily at Φ = 0.17 than at Φ = 0.34. It can also be seen that there is a high level of reaction completion in the Φ = 0.17 case at the upstream end of the flame front, evidenced by high levels of H_2O there. Contrastingly, combustion at the higher equivalence ratio results in H_2O production that is dispersed throughout the flame structure and near the upper wall; this indicates slower mixing and reaction rates. High H_2O concentrations near the upper wall are due mainly to action of the axial vortices shed from the corners of the compression ramp, which tend to carry combustion products toward the centerline of the upper wall. It is likely that the greater expansion of the fuel jet at Φ = 0.34 interferes with flameholding and flow recirculation just downstream of the injector, resulting in weaker flame attachment and the shifting of the hottest part of the flame downstream.

D. Data Comparisons: Reactant Mixing with Combustion, Φ=0.17 and Φ=0.34

Figure 15 plots LES/RANS averaged and RANS injector wall pressures along with experimentally measured values. Overall, fairly good agreement is obtained, with the numerical results predicting the positions of pressure increase well. For Φ = 0.17, the RANS solution predicts a greater pressure rise due to greater heat release near the injector, which gives better agreement with experimental data. However, the opposite is true for Φ = 0.34, as the RANS method predicts a more delayed pressure rise near the wall compared to LES/RANS and experimental results. Figure 7 confirms this: there is stronger flame anchoring near the injector in the LES/RANS result, whereas the RANS result predicts strong reaction and mixing in the shear layer between the fuel plume and the core flow further downstream in the combustor (the flame, however, is still weakly anchored at the injector).

Figure 16 compares LES/RANS and RANS temperature distributions at Φ = 0.17 with experimental CARS data at three planes downstream of the injector exit plane: x/H = 6, x/H = 12, and x/H = 18.   Actual data locations are shown as small black squares. To arrive at the images presented in the figure, the CARS data at those locations was interpolated to a uniform 200x200 grid spanning each plane. Tecplot's kriging interpolation methods were used. A similar interpolation was applied to the LES/RANS data (fourth column) to enable a more consistent visual comparison.   The temperature at each station is over-predicted significantly by the RANS approach but is in much better agreement with the CARS data for the LES/RANS method.   The displacement effect of the reacting gas plume in the y direction (away from the injector wall) appears to be under-estimated at x/H = 12 by the LES/RANS method. This trend is consistent with the pressure distributions shown in Fig. 15.

Hydrogen mole fraction distributions from CARS measurements are compared with LES/RANS and RANS predictions in Fig. 17.   The LES/RANS and RANS solutions are generally symmetric; the experimental results indicate a degree of distortion of the jet plume that is not solely due to the sparsity of the data set.   The general rate of mixing is well-predicted by the LES/RANS model. The RANS predictions imply a more rapid rate of jet mixing and more complete combustion downstream of the injector ramp.

Instantaneous axial density gradient contours at the X-Y centerplane are compared with focusing Schlieren images in Fig. 18 for the combusting case at Φ = 0.17. Also shown is a computed image corresponding to the Φ = 0.34 combusting case. The deflection of the shear layer into the core flow for the Φ = 0.17 case results in the formation of a shock wave that then reflects from the upper wall. These waves comprise the leading edge of the

shock train discussed earlier. Turbulent structures in the shear layer just downstream of the ramp trailing edge are shown in the Schlieren image but are absent in the calculation. This is a consequence of the absence of inflow boundary-layer forcing in the present simulations. The hydrogen jet appears to penetrate further into the wake of the ramp in the calculation, but this trend may be a consequence of comparing two uncorrelated snapshots. The hydrogen jet expands more rapidly for the $\Phi = 0.34$ case; the Mach disk created as the fluid within the jet re-compresses eventually reflects from the lower wall. A shear layer that also exhibits characteristic Kelvin-Helmholz structures is formed downstream of this compression wave. The displacement of the upper shear layer into the core flow appears to be similar to that exhibited in the $\Phi = 0.17$ solution, but it is clear that the shock train is positioned further upstream. This may indicate that the reactive shear layer in the $\Phi = 0.34$ spreads more in the lateral (z) direction than in the $\Phi = 0.17$ case.

Time-averaged stereoscopic PIV velocity magnitude contours at x/H = 12 are compared with LES/RANS and RANS predictions for the $\Phi = 0.17$ reacting case in Figure 19. As in the mixing case, seeding is through the hydrogen jet, and only those regions of the flow impacted directly by the jet yield accurate PIV results. The experimental plume is displaced further away from the injector wall (top) than indicated in the LES/RANS data. The RANS predictions are in closer agreement with the plume width, but the core fluid is significantly accelerated, implying that mixing rates are over-predicted. In contrast, the LES/RANS method predicts the core mixing rates much more accurately.

Qualitative comparisons with OH-PLIF images are shown in Figure 20 for the x/H = 12 plane at $\Phi = 0.17$. In the top part of the figure, ensemble-averages of fluorescence intensity (2000 images) are compared with time averaged OH mass-density predictions from the LES/RANS and RANS models. The bottom part of the figure compares an instantaneous snapshot from the OH-PLIF data base with an OH mass density snapshot from the LES/RANS simulation. The computational and experimental images are scaled independently, with the range for the contour levels encompassing those of both the instantaneous and time-averaged images. This shows the degree of variation between the time-averaged result and the instantaneous value and clearly indicates the influences of finite rates of reactant mixing and large turbulence-induced strain rates in disrupting the continuous flame front exhibited in the RANS solution. Peak average OH concentrations are located toward the injector wall and are coincident with the outer part of the core mixing region evidenced in Figs. 17 and 19. The eddy sizes as predicted by the LES/RANS model seem to be in close agreement with those indicated in the OH-PLIF data, though locally, higher relative OH concentrations are observed in the predictions of the eddies. This trend could again be a result of comparing uncorrelated images. The OH-PLIF database is substantial, encompassing the region from just upstream of the injector rear plane (x/H = 0) to approximately x/H = 25 at $\Phi = 0.17$ and $\Phi = 0.34$. Future work will concentrate on additional comparisons with this data and on the use of the experimental and computational results to analyze the flame structure in more detail.

VIII.   Conclusions

Comparisons between Generation I (RANS) and Generation II (hybrid LES/RANS) numerical simulation methodologies and experimental measurements have been performed for reacting and non-reacting experiments conducted at the University of Virginia's Scramjet Combustion Facility. The flowpath was configured with a short isolator, single finite-width gaseous hydrogen ramp/injector, and a divergent combustor and extender in order to accommodate higher equivalence ratios and hydrocarbon fuels in the future. Numerical and experimental data were obtained for the two equivalence ratios of $\Phi = 0.17$ and $\Phi = 0.34$. Experimental data gathered included wall static pressure measurements, focusing Schlieren images, stereoscopic particle image velocimetry (SPIV) measurements, coherent anti-Stokes Raman scattering (CARS) measurements, hydroxyl planar laser induced fluorescence (OH-PLIF) images, and line-of-sight wavelength modulation spectroscopy (WMS) profiles. The computations were essentially performed in a 'blind' manner, as only wall-pressure data at $\Phi = 0.17$ was available prior to the completion of the simulations. The results therefore represent a first cut at simulating these complex flows without any adjustments in the basic models or numerical methods being made to facilitate better agreement with experimental observations. The LES/RANS model directly captures effects due to turbulent mixing at larger scales and local straining of the flame due to resolved turbulence, leading to better agreement with experimental results in the near field of the injector. The LES/RANS model does slightly under-predict the displacement effects of reacting plumes and low-momentum regions caused by shock / boundary layer interactions. As such features are impacted directly by heat release, it may be conjectured that the overall level of heat release may be under-predicted by this model. In contrast, the RANS model predicts blockage effects somewhat better but over-predicts the flame temperature and the rate of reactant mixing and consumption. The LES/RANS techniques are also able to capture large-scale unsteady flow features, such as shock-train oscillation, to a much higher fidelity than the RANS models.

Future work will focus on further analysis and comparison with other measurement data as it becomes available. Sensitivities to variations in the model closures will also be investigated, and simulations of a new design that contains an isolator section and a straight section that separates the combustor from the extender will also be performed.

Acknowledgments

References

[1]McDaniel, James C., Chelliah, Harsha, and Goyne, Christopher P. "US National Center for Hypersonic Combined Cycle Propulsion: An Overview," AIAA Paper 2009-7280.

[2]Wilcox, David C., *Turbulence Modeling for CFD*, 3rd ed., DCW Industries, Inc., La Canada, CA, 2006, Sxn. 1.3.2.

[3]Goyne, C. P., Rodriguez, C. G., Krauss, R. H., McDaniel, J. C., and McClinton, C. R. "Experimental and Numerical Study of a Dual-Mode Scramjet Combustor," *Journal of Propulsion and Power*, Vol. 22, No. 3, 2006, pp. 481-489.

[4]Georgiadis, N. J. et al. "Wind-US Code Physical Modeling Improvements to Complement Hypersonic Testing and Evaluation" AIAA Paper 2009-193.

[5]Vyas, M. A., Engblom, W. A., Georgiadis, N. J., Trefny, C. J., and Bhagwandin, V. A. "Numerical Simulation of Vitiation Effects on a Hydrogen-Fueled Dual-Mode Scramjet" AIAA Paper 2010-1127.

[6]Fulton, J.A., Edwards, J.R., Goyne, C.P., McDaniel, J.C., and Rockwell, R. "Numerical Simulation of Flow in a Dual-Mode Scramjet Combustor" AIAA Paper 2010-3714.

[7]Hassan, H., Edwards, J.R., and Fulton, J.A. "Role of Turbulence Modeling in Supersonic Combustion" AIAA Paper 2011-5829.

[8]Jachimowski, C. J. "An Analysis of Combustion Studies in Shock / Expansion Tunnels and Reflected Shock Tunnels, NASA TP-3224, 1992.

[9]Edwards, J.R. "A Low-Diffusion Flux-Splitting Scheme for Navier-Stokes Calculations," *Computers and Fluids*, Vol. 26, No. 6, 1997, pp. 635-659.

[10]Ducros, F., Ferrand, V., Nicaud, F., Weber, C., Darracq, D., Gachareiu, C., Poinsot, T. "Large-Eddy Simulation of the Shock / Turbulence Interaction" *Journal of Computational Physics*, Vol. 152, No. 2., 1999, pp. 517-549.

[11]Menter, F.R. "Two Equation Eddy Viscosity Turbulence Models for Engineering Applications," *AIAA Journal*, Vol. 32, No. 8, 1994, pp. 1598-1605.

[12]Gieseking, D.A, Choi, J.-I., Edwards, J.R., and Hassan, H.A. "Compressible Flow Simulations using a New LES/RANS Model" *AIAA Journal,* Vol. 49, No. 10, 2011, pp. 2194-2209.

[13]Lenormand, E., Sagaut, P., Ta Phuoc, L., and Comte, P., "Subgrid-Scale Models for Large-Eddy Simulations of Compressible, Wall-Bounded Flows," *AIAA Journal*, Vol. 38, 2000, pp. 1340-1350.

[14]Rockwell, R.D., Goyne, C.P., Rice, B.E., Tatman, B.J., Smith, C., Kouchi, T., McDaniel, J.C., Fulton, J.A., and Edwards, J.R. "Close-Collaborative Experimental and Computational Study of a Dual-Mode Scramjet Combustor," To be presented at the 50th Aerospace Sciences Meeting and Exhibit, Nashville, TN, Jan., 2012.

[15]Boles, J.A., Edwards, J.R., and Baurle, R.A. "Multi-wall Recycling / Rescaling Method for Inflow Turbulence Generation" AIAA paper 2010-1099, Jan. 2010.

[16]Magnotti, G., Cutler, A.D., Danehy, P.M., "Dual-Pump CARS Measurements in a Supersonic Combusting Free Jet," To be presented at the 50th AIAA Aerospace Sciences Meeting, Nashville, TN, Jan. 2012.

[17]Cutler, A.D., Magnotti, G., Cantu, L., Gallo, E., Danehy, P.M., Rockwell, R., Goyne, C., and McDaniel, J., "Dual-Pump CARS Measurements in the University of Virginia's Dual-Mode Scramjet: Configuration "A"." To be presented at the 50th AIAA Aerospace Sciences Meeting, Nashville, TN, Jan. 2012

[18]O'Byrne, I. Stotz, A. Neely, R. Boyce, N. Mudford, and A. Houwing, "OH PLIF Imaging of Supersonic Combustion Using Cavity Injection," AIAA 2005-3357, May, 2005.

[19]Weinstein, L.M. , "Review and Update of Lens and Grid Schlieren and Motion Camera Schlieren,*" The European Physical Journal Special Topics*, Vol. 182, pp. 65-95, 2010.

[20]Schultz, I.A., Goldenstein, C.S., Jeffries, J.B., and Hanson, R.K. "Tunable Diode Laser Absorption Sensor for in situ Determination of Combustion Evolution in Scramjet Ground Testing" Abstract submitted for presentation at the 29th AIAA Aerodynamic Measurement and Ground Testing Conference, 2012.
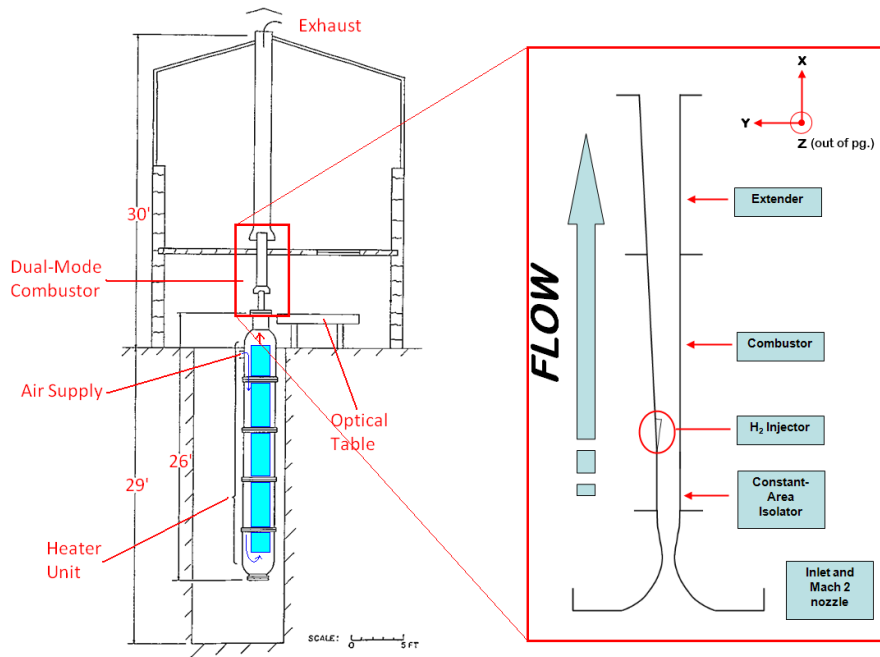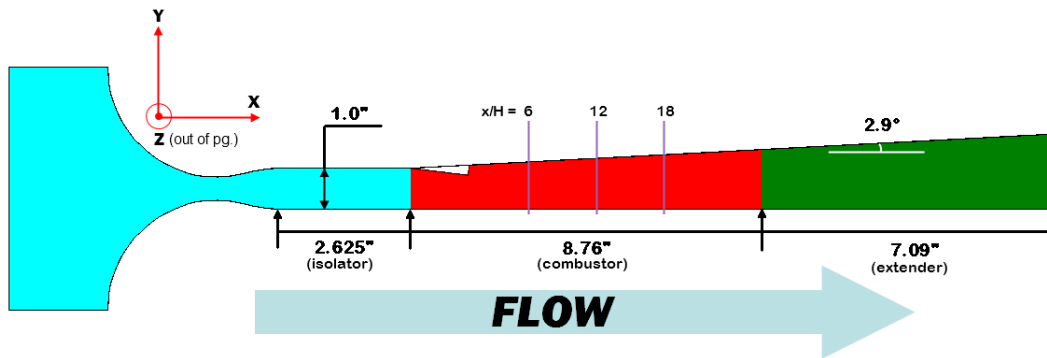
Figure 1. UVa SCF facility layout.
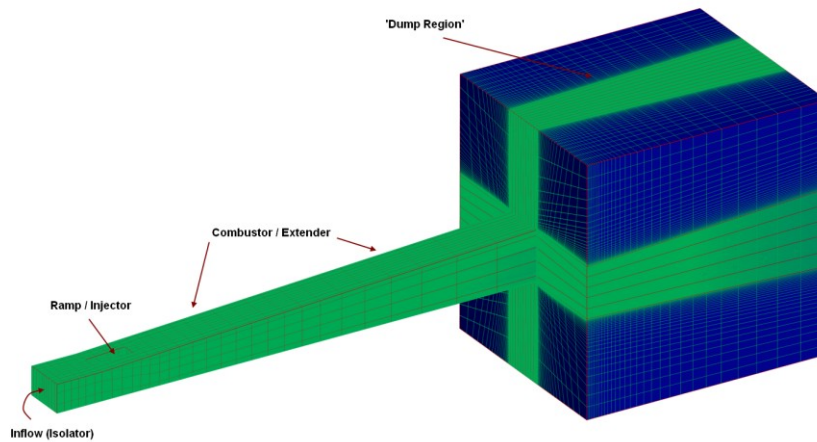

Figure 2. Configuration A Flowpath.

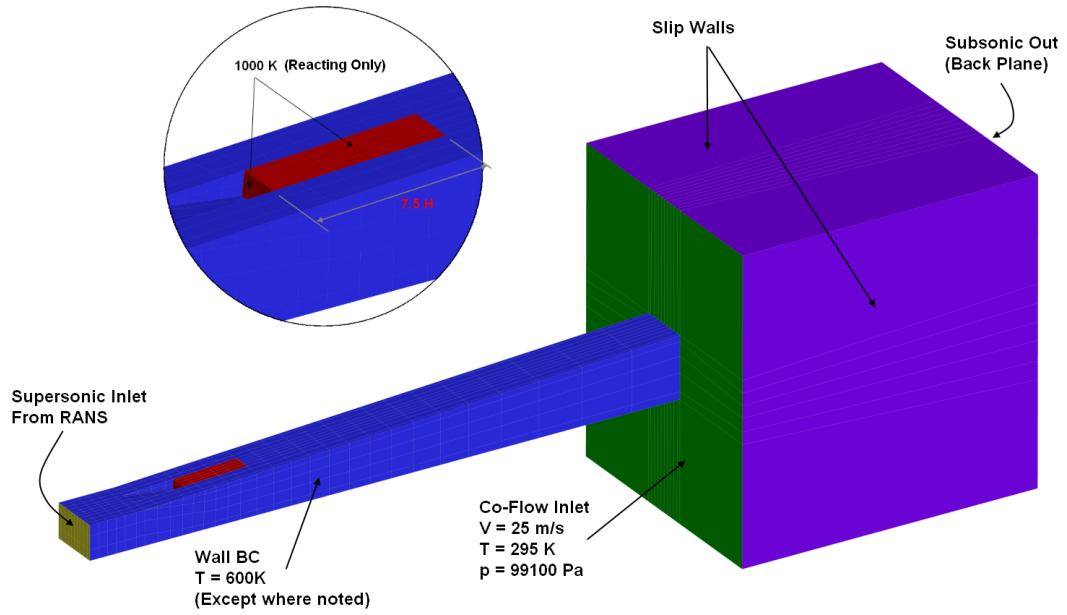Figure 3. Configuration A Mesh Blocking Arrangement.
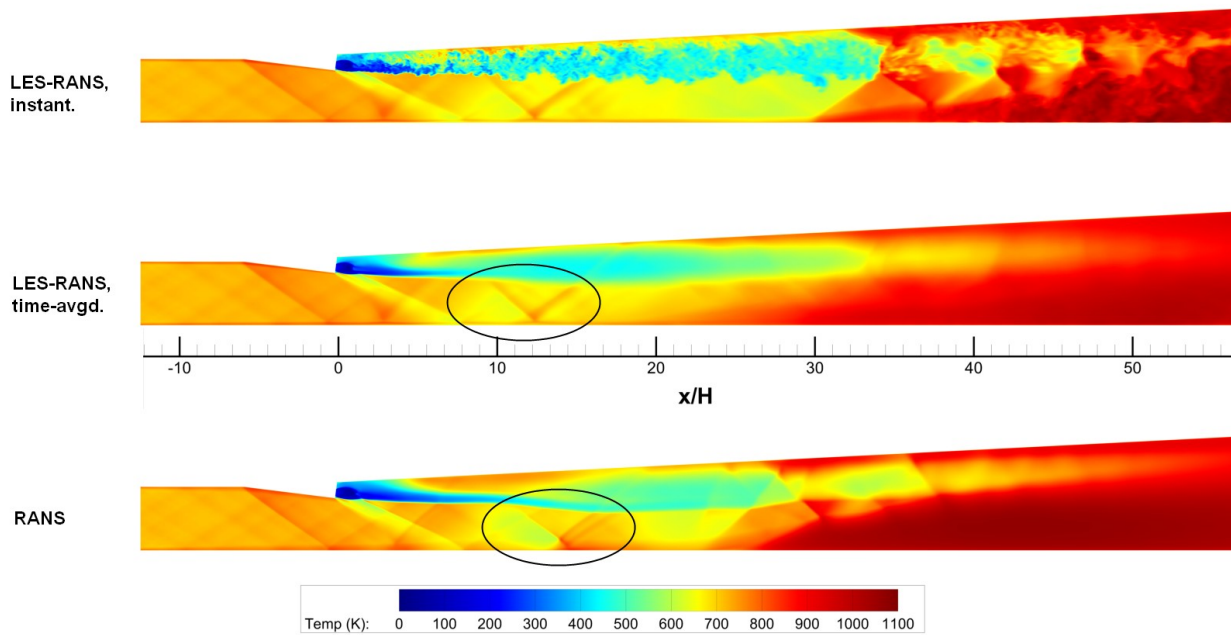
Figure 4. Boundary Condition Detail.

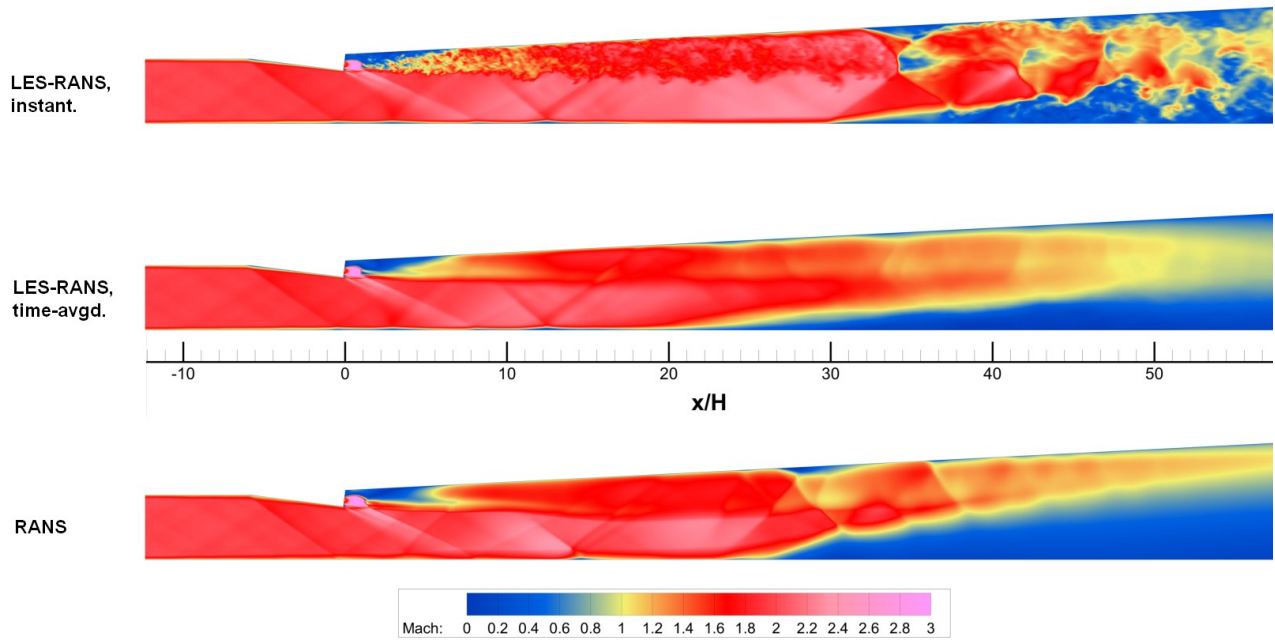**Figure 5. Centerplane Contours of Temperature, Φ = 0.17 mixing.**

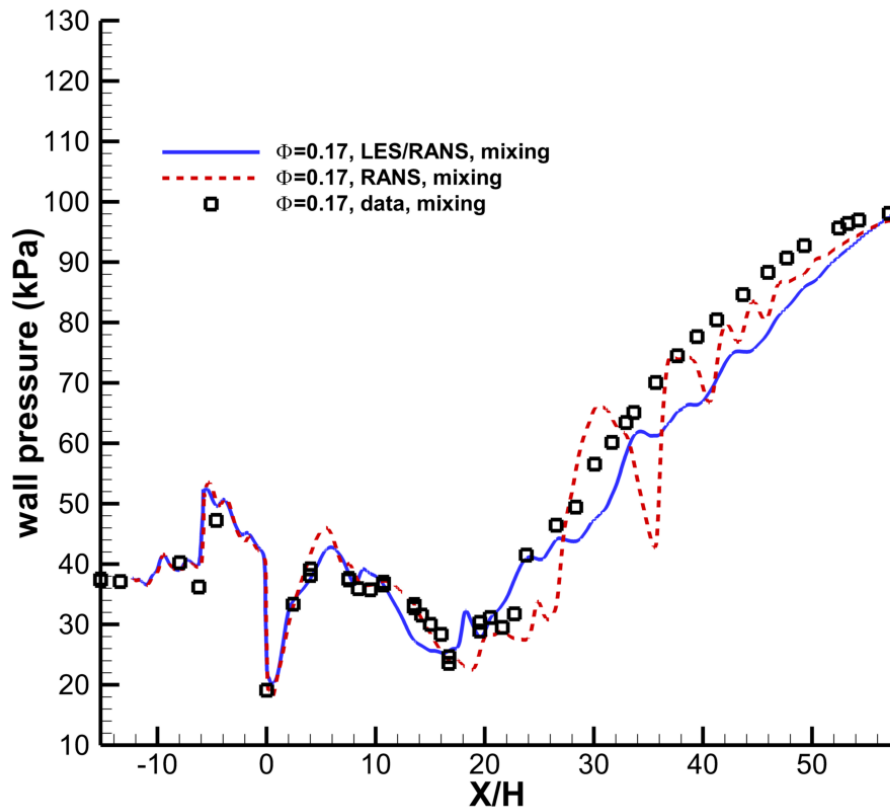**Figure 6. Centerplane Contours of Mach Number, Φ = 0.17 Mixing.**

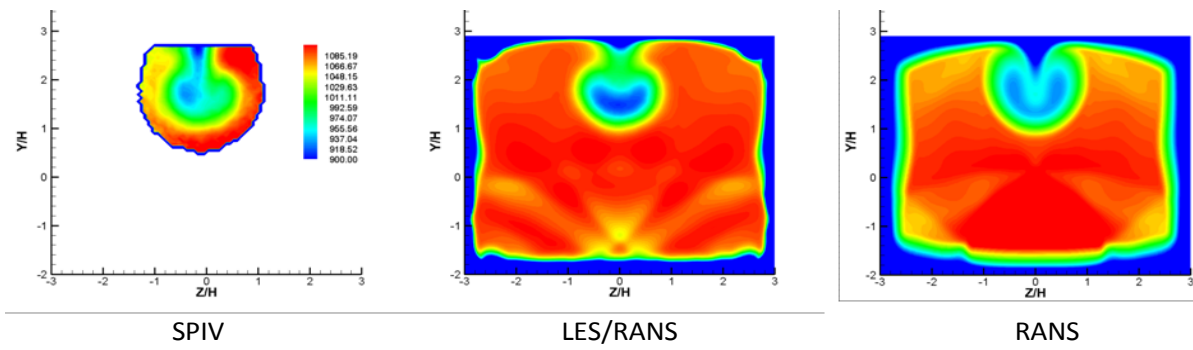**Figure 7. Comparison of Injector Wall Static Pressures, Φ = 0.17 Mixing.**

| SPIV | LES/RANS | RANS |

Figure 8. Numerical Velocity Magnitude vs. SPIV Measurements. Mixing Case, ϕ=0.17.
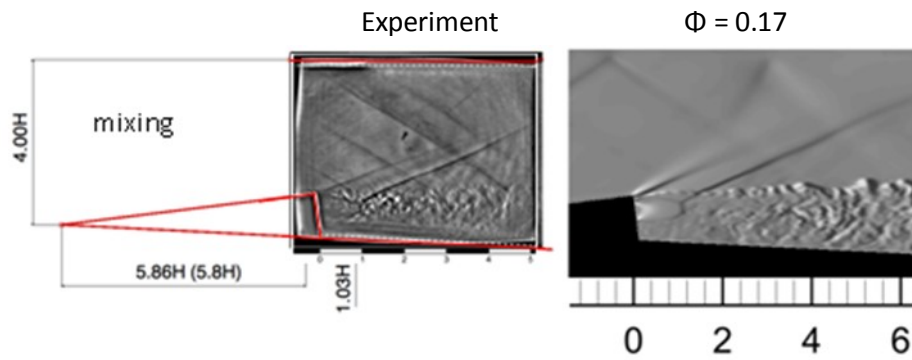
Figure 9. Instantaneous Density Gradient Images versus Focusing Schlieren Measurements (Mixing Case).
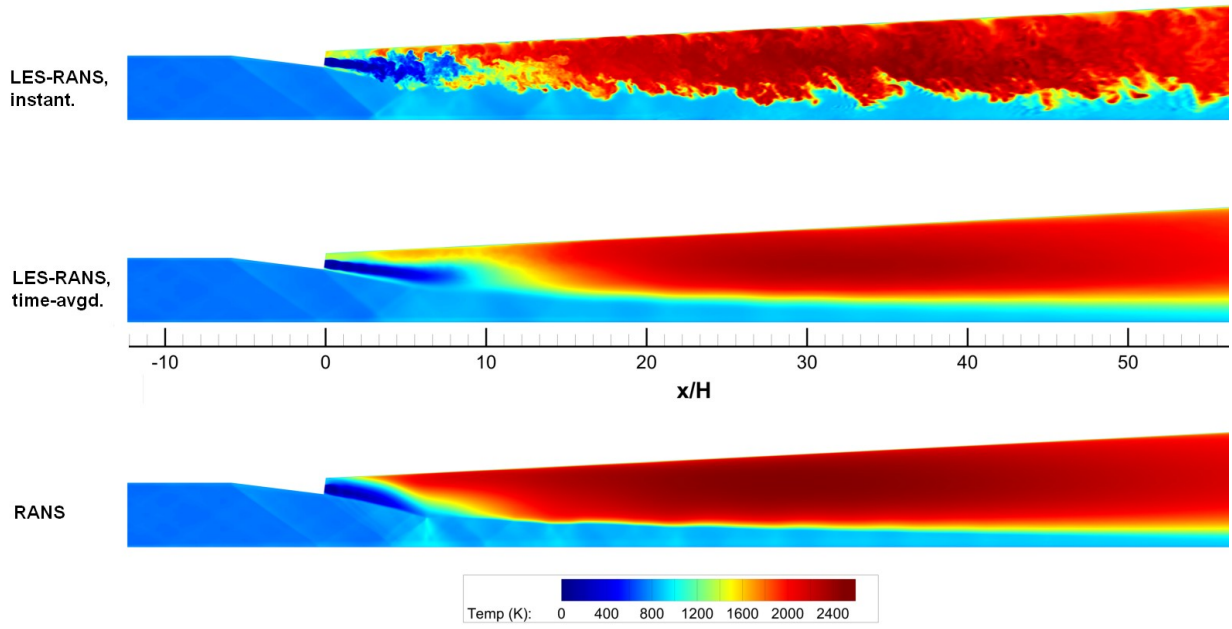
Figure 10. Centerplane Contours of Temperature, Φ = 0.17 Reacting.
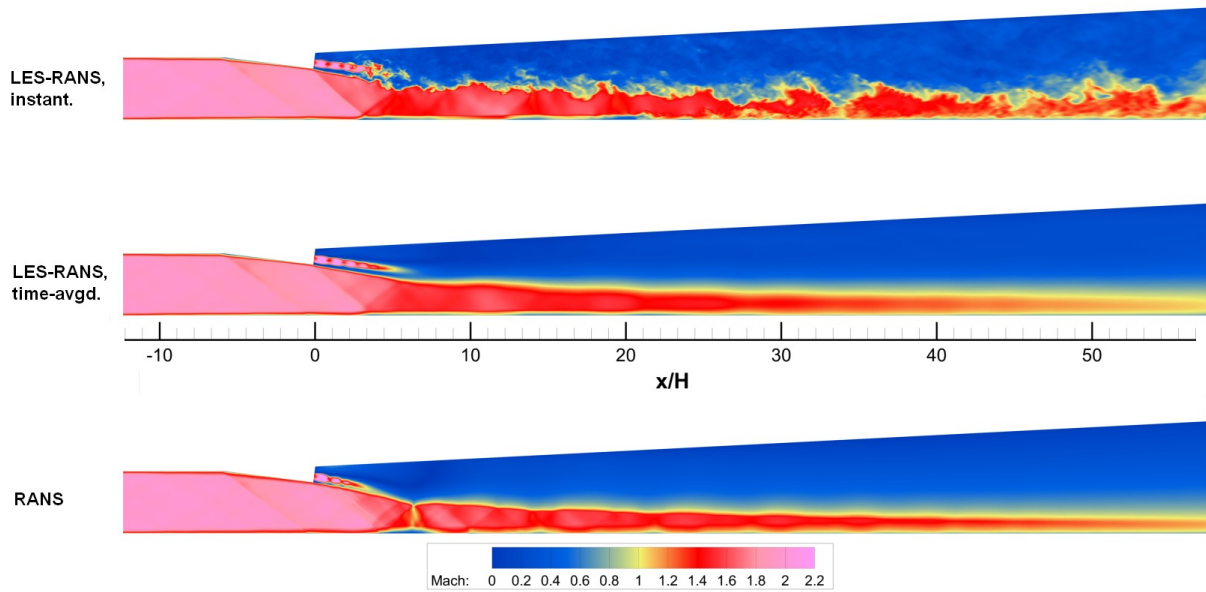
Figure 11. Centerplane Contours of Mach Number, Φ = 0.17 Reacting.
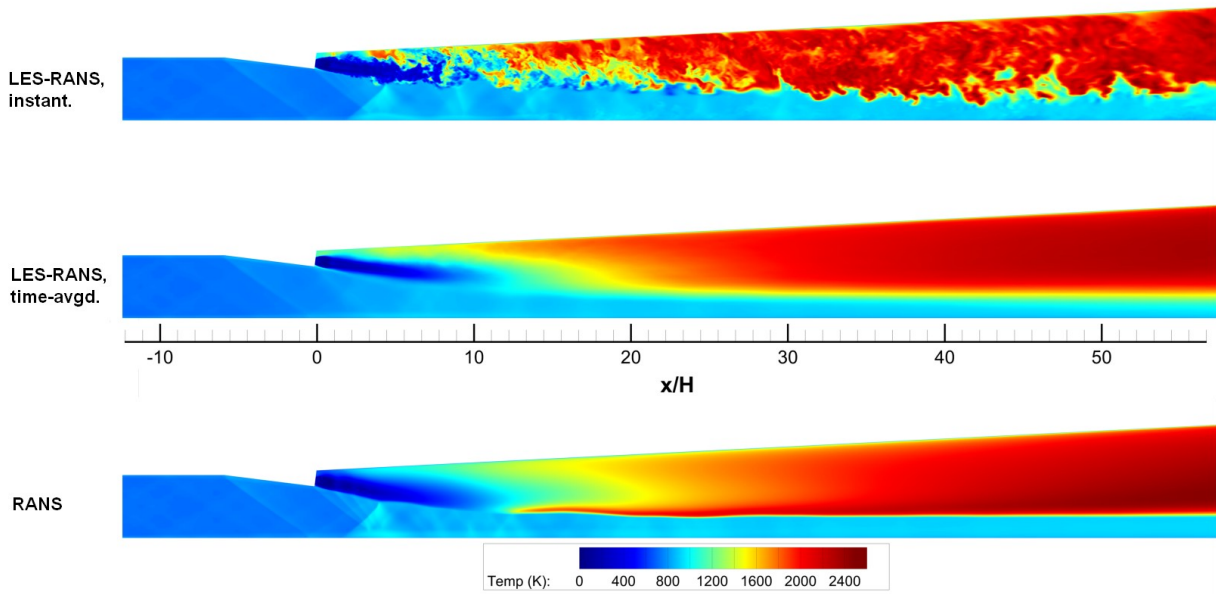
Figure 12. Centerplane Contours of Temperature, Φ = 0.34 Reacting.
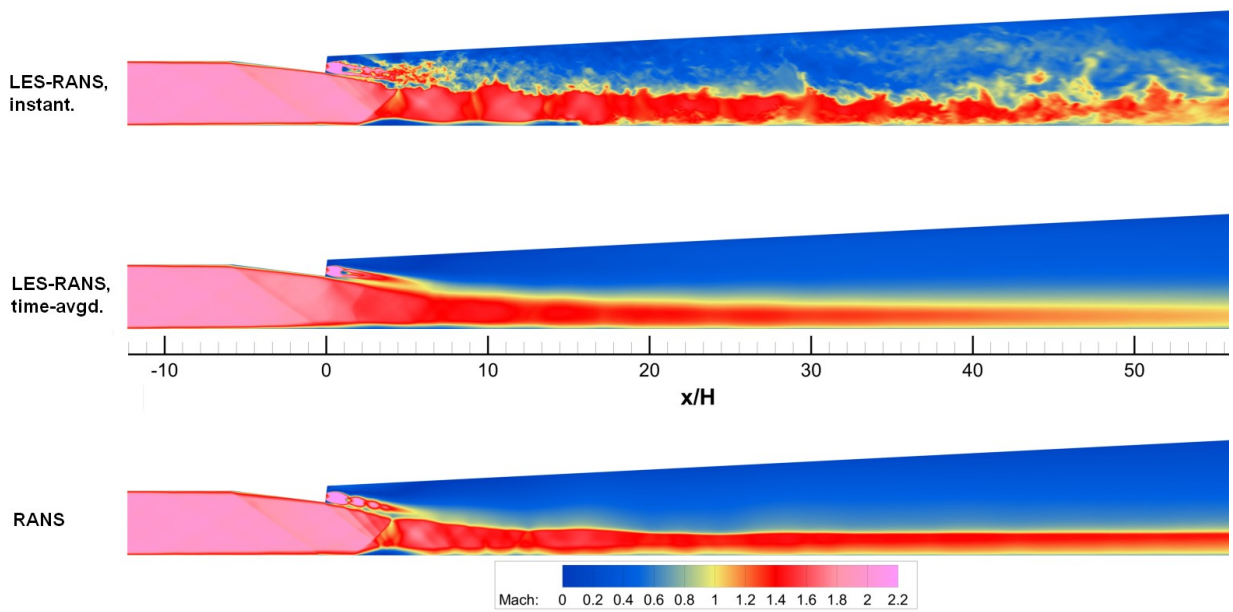
Figure 13. Centerplane Contours of Mach Number, Φ = 0.34 Reacting.
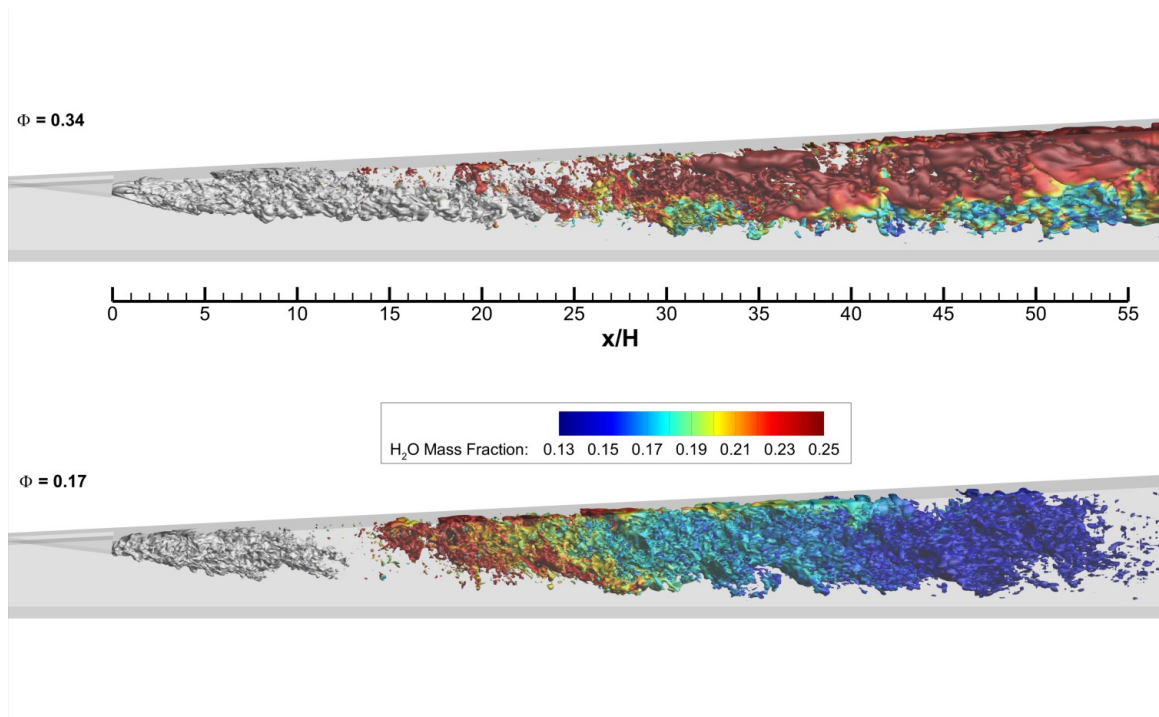
Figure 14. Isosurfaces of H₂ Mass Fraction (0.1) in grey and Temperature (2200 K) Colored by H₂O Mass Fraction.
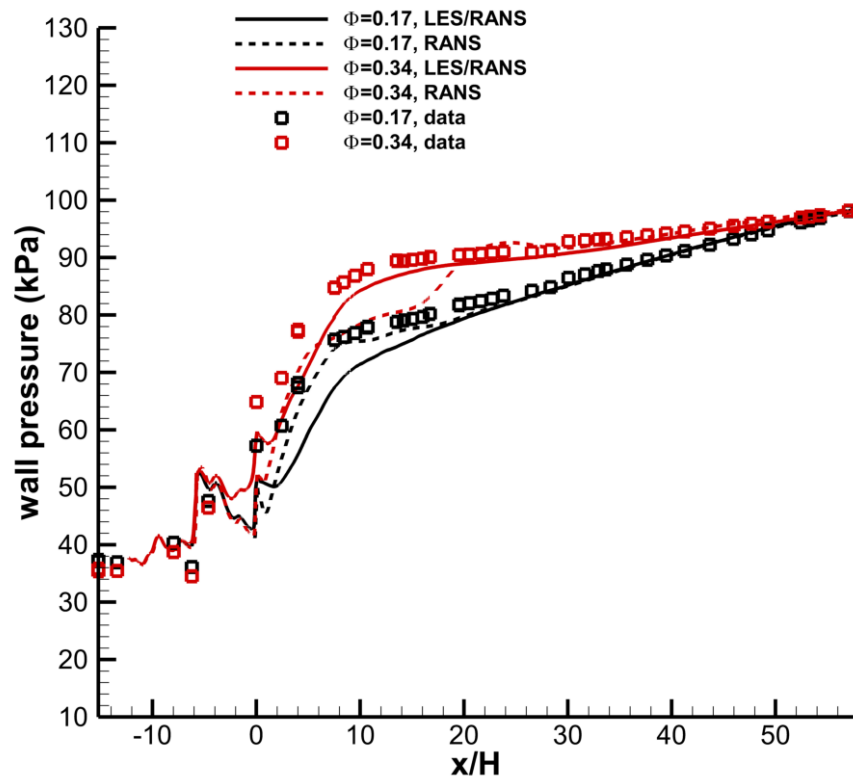
Figure 15. Wall Static Pressure Comparison, Reacting Cases.
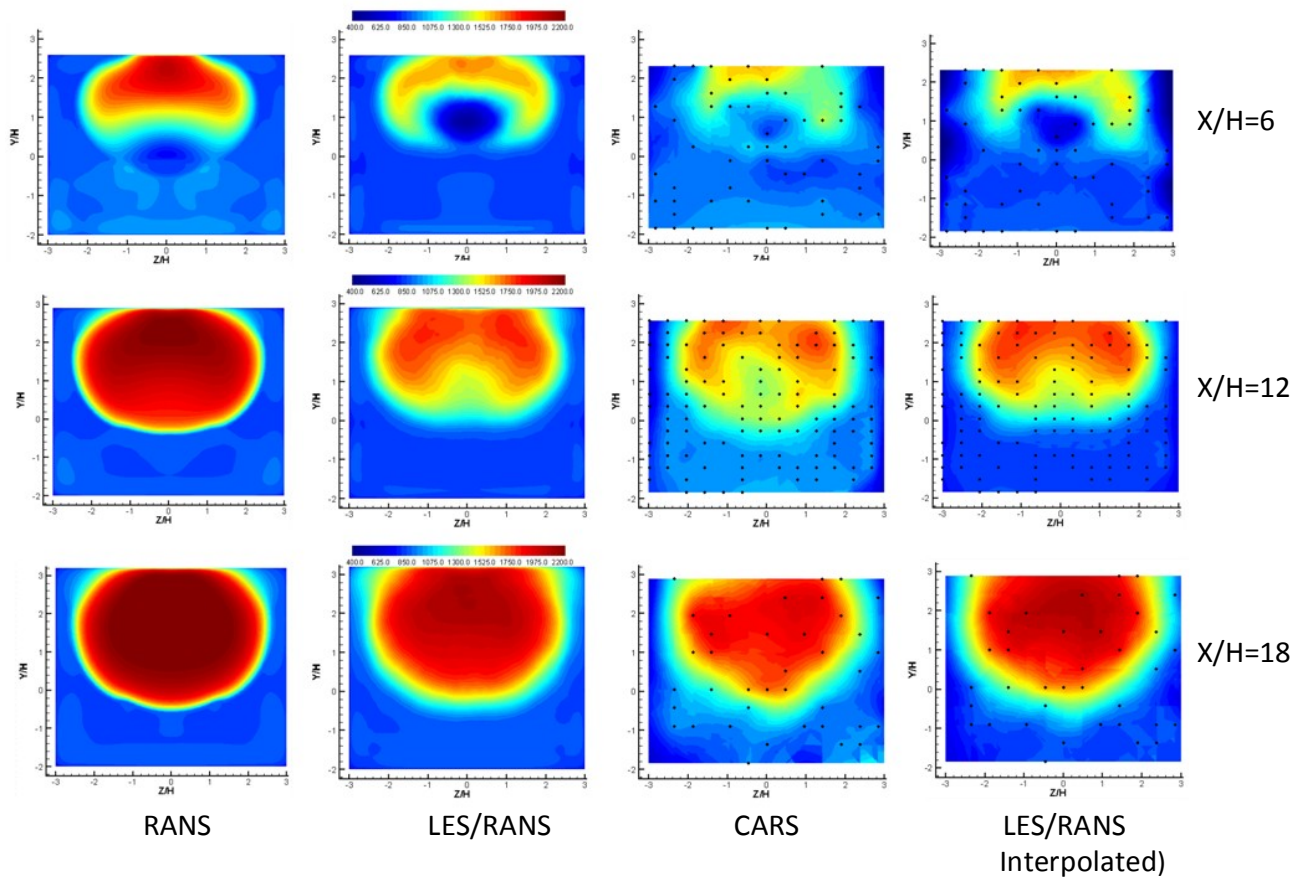
Figure 16. Comparison with CARS temperature measurements at x/H = 6, 12, and 18.
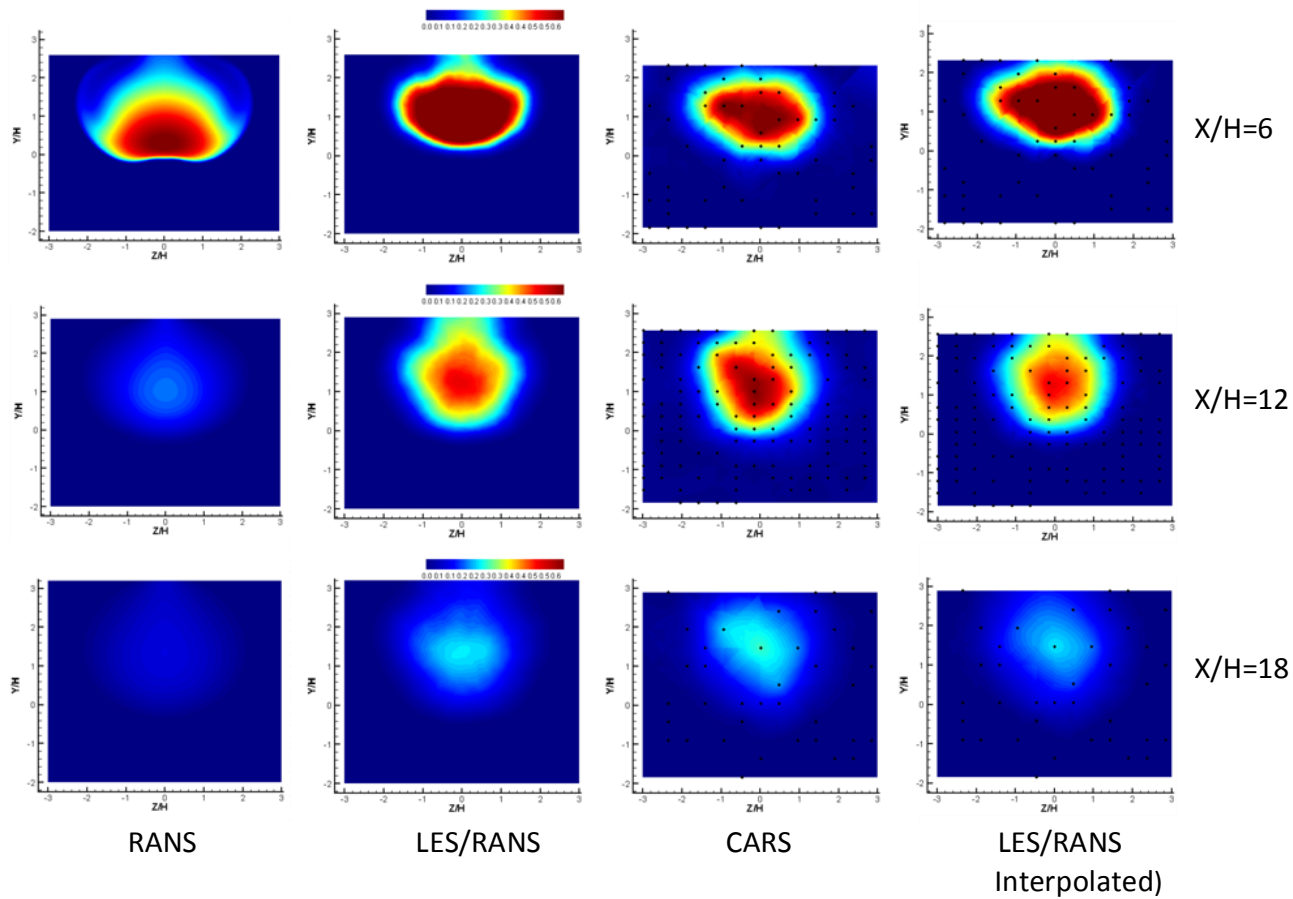
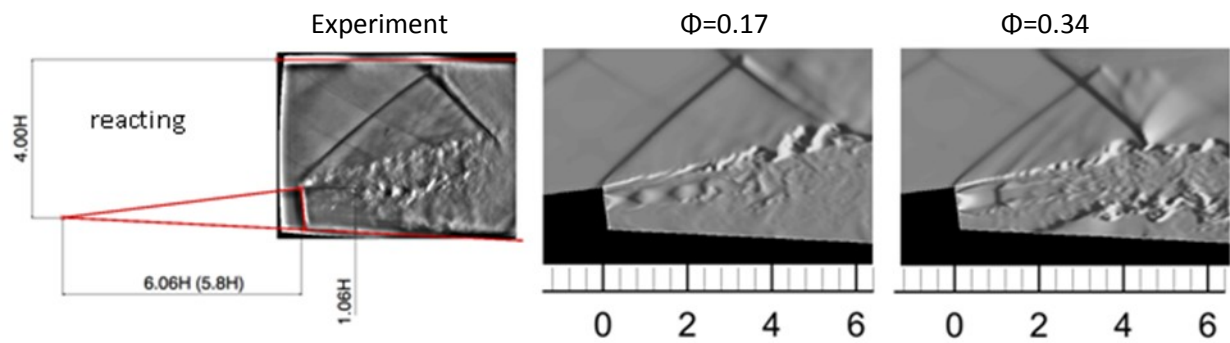**Figure 17. Comparison with CARS H$_2$ mole-fraction measurements at x/D = 6, 12, and 18.**

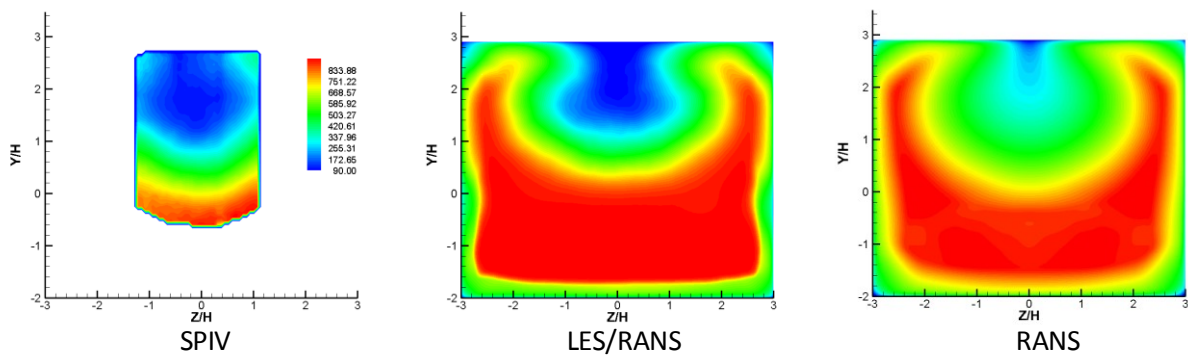**Figure 18. Instantaneous Density Gradient Images versus Focusing Schlieren Measurements (Reacting Cases)**

Figure 19. Numerical Velocity Magnitude vs. SPIV Measurements. Reacting Case, φ=0.17.
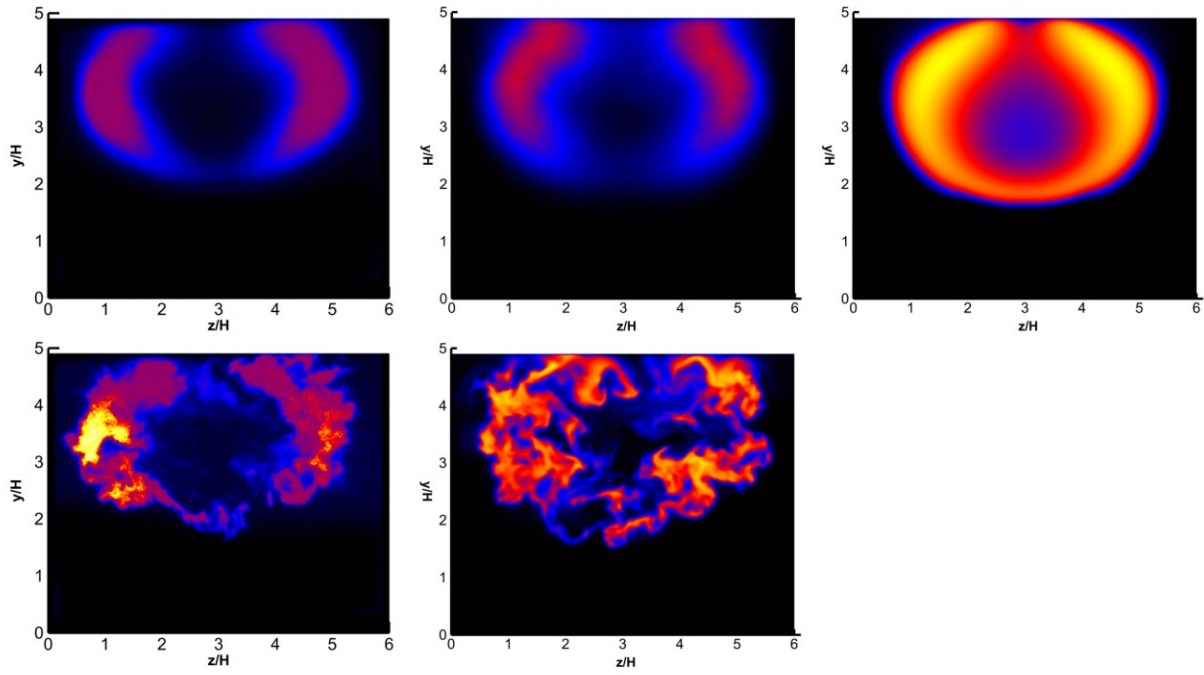
Figure 20. Comparison with OH-PLIF Images (top: time averaged images; bottom: instantaneous images; left to right: OH-PLIF, LES/RANS, RANS).